A genome-wide optical pooled screen reveals regulators of cellular antiviral responses

Rebecca J. Carlson[a,b] (ID), Michael D. Leiken[b], Alina Guna[c] (ID), Nir Hacohen[b,d,1] (ID), and Paul C. Blainey[b,e,f,1] (ID)

The infection of mammalian cells by viruses and innate immune responses to infection are spatiotemporally organized processes. Cytosolic RNA sensors trigger nuclear translocation of the transcription factor interferon regulatory factor 3 (IRF3) and consequent induction of host immune responses to RNA viruses. Previous genetic screens for factors involved in viral sensing did not resolve changes in the subcellular localization of host or viral proteins. Here, we increased the throughput of our optical pooled screening technology by over fourfold. This allowed us to carry out a genome-wide CRISPR knockout screen using high-resolution multiparameter imaging of cellular responses to Sendai virus infection coupled with in situ cDNA sequencing by synthesis (SBS) to identify 80,408 single guide RNAs (sgRNAs) in 10,366,390 cells—over an order of magnitude more genomic perturbations than demonstrated previously using an in situ SBS readout. By ranking perturbations using human-designed and deep learning image feature scores, we identified regulators of IRF3 translocation, Sendai virus localization, and peroxisomal biogenesis. Among the hits, we found that ATP13A1, an ER-localized P5A-type ATPase, is essential for viral sensing and is required for targeting of mitochondrial antiviral signaling protein (MAVS) to mitochondrial membranes where MAVS must be localized for effective signaling through retinoic acid-inducible gene I (RIG-I). The ability to carry out genome-wide pooled screens with complex high-resolution image-based phenotyping dramatically expands the scope of functional genomics approaches.

CRISPR screening | RIG-I | IRF3 | high-content imaging | Sendai

Host cell responses to viral infection are conserved processes critical for defense against established and emerging viruses. Intracellular responses to RNA virus infection are mediated by innate immune signaling pathways that begin with binding of viral RNA by the pattern recognition receptor (PRR) RIG-I or melanoma differentiation-associated protein 5 (MDA5). The PRRs in turn trigger phosphorylation and nuclear translocation of the transcription factor IRF3, which induces transcription of the interferon antiviral immunity program (1). Activating mutations in these PRRs and increased spontaneous IRF3 translocation are associated with autoimmune syndromes (2, 3), and activation of PRRs such as RIG-I, on the other hand, can boost antitumor responses (4). Given the importance of IRF3 translocation, a better understanding of genes that regulate its activation and translocation may contribute to design of therapeutics to boost antiviral immunity, dampen autoimmunity, or support antitumor immunity.

While a number of genome-wide CRISPR screens for control of virus infection have been performed, most have assayed cell fitness (5–12) or viral replication (13, 14) in response to cellular infection by a pathogenic virus. More recently, pooled genome-wide screens have examined interferon induction in response to interferon treatment (15–17) or Sendai virus (SeV) infection (18); however, none have been able to examine IRF3 translocation directly, a critical step in the sensing pathway, because pooled genetic screens are not typically compatible with subcellular imaging assays. While a kinome-wide image-based arrayed siRNA screen for IRF3 translocation has been performed (19), genome-wide arrayed screens have not become routine due to the high cost and labor investment required for cellular imaging in an arrayed format.

We recently developed a method to perform pooled image-based screens by linking single-cell image-based phenotypes to perturbation identity in mammalian cell libraries (20, 21). Using targeted in situ sequencing, this method demultiplexes entire cell libraries containing genetic CRISPR perturbations following phenotyping. In order to scale the method to the genome-wide level, we improved the throughput by over fourfold by 1) using a microscope system with reduced stage movement latency (Nikon Imaging Software Elements with a Ti2 microscope rather than Micro-Manager software with a Ti-E microscope) and 2) completing tiled image acquisitions for each color channel before reconfiguring the microscope for the next color channel in order to eliminate time-intensive

Significance

Our study demonstrates scaling of optical pooled screening to the genome-wide level. Profile-based screening is a uniquely powerful phenotype-based genetic tool that enables retrospective assignment of genetic perturbations to multiple phenotypic categories. Here, we demonstrated the power of optical pooled screening to support analysis of 80,000 perturbations from single-cell images of about 10 million cells. We leverage the results to generate insights into innate immune responses to viral infection including the essentiality of ATP13A1 function for signaling through RIG-I/DDX58.

optical filter switching at each field of view. The second advance degraded raw alignment precision across channels, necessitating development of fast and accurate computational image alignment across multicentimeter scales (*SI Appendix*, Fig. S1*E*). In addition, while we previously only assayed two to four phenotyping channels due to incompatibility of other channels with Illumina's four-color sequencing-by-synthesis reagents (20, 22), here we assayed as many as seven phenotyping channels at a time by taking advantage of the higher local optical intensity of the in situ sequencing signals and applying our higher-throughput data acquisition protocol for phenotyping with commercially available reagents. Our multiparameter screen identified regulators of IRF3 translocation, peroxisome biogenesis, and spatial localization of SeV, a paramyxovirus known to induce strong interferon responses (23), and demonstrates the feasibility of optical pooled screening at the genome-wide scale to discover complex, multiparameter phenotypes.

Results

A Genome-Wide Optical Pooled Screen Identifies Regulators of IRF3 Translocation. We performed a genome-wide optical pooled screen using a lentivirus library of 80,408 sgRNAs targeting over 20,000 genes, with 454 nontargeting sgRNAs. HeLa-TetR-Cas9 cells were stably transduced with BFP-PTS1 (*SI Appendix*, Fig. S1 *A* and *B*), a peroxisomal marker, and were infected at an MOI of 0.05 with the sgRNA library. Following 7 days of doxycycline Cas9 induction, cells were infected with the SeV Cantell strain at an MOI of 10 for 15 hours prior to imaging (Fig. 1*A*). We then performed multiplexed immunofluorescence imaging, assessing two organelles critical to antiviral signaling—peroxisomes and mitochondria (24)—the RNA receptors MDA5 and RIG-I, pIRF3, SeV itself, and DNA (DAPI) in all cells (Fig. 1*C*) before performing reverse transcription, padlock targeting of cDNA, RCA, and in situ sequencing by synthesis (SBS) to detect sgRNAs as previously described (21, 25). We performed 12 cycles of in situ SBS to read out all sgRNAs (Fig. 1*D*). Due to the high intensity of the in situ SBS signal relative to immunofluorescence staining, we titrated the immunofluorescence reagents that produced signal in the phenotyping channels that overlapped with SBS spectra to mitigate interference with base calling (Fig. 1*B*). This strategy enabled the acquisition of as many as seven channels of phenotyping data without using custom-modified antibodies (22), an advancement over the two to four phenotyping channels previously demonstrated using optical pooled screening, without the need for specialized reagents (20). Images of single cells from our genome-wide pooled screen showed robust translocation of phosphorylated IRF3 in nontargeting control cells, while RIG-I, MAVS, and IRF3 knockouts profoundly impair translocation across multiple sgRNAs (Fig. 1 *E* and *F*) and were the three highest scoring genes in the screen (Fig. 1 *G–I* and Dataset S1). To confirm the results of our primary screen, we performed focused secondary pooled screens (using 6 sgRNAs/gene) of 342 genes that scored for either increasing or decreasing IRF3 translocation in our genome-wide screen using antibody staining or an IRF3 reporter (Fig. 1*G* and Datasets S2 and S3). Secondary screen translocation scores were well correlated with translocation scores from the primary genome-wide screen (Fig. 1*H*), underscoring the considerable statistical power achieved for IRF3 translocation in the primary genome-wide screen. 51 genes were confirmed by stringent criteria to score in both of our secondary screens, including the known pathway members MAVS, DDX58, RNF135, and IRF3 (26), Fig. 1*I*.

We next examined regulators of IRF3 translocation confirmed by secondary screening using STRING analysis (27) and found that the majority are predicted interactors (minimum confidence 0.4, 13/24 of the genes found to decrease translocation, $P = 8.16e-7$, Fig. 2*A*, and 18/27 genes increase translocation, $P = 1.11e-16$, Fig. 2*B*). Among genes found to decrease translocation, we identified a set containing genes known to be involved in RIG-I induction of interferon, as well as genes involved in ubiquitin transferase activity, which is intriguing since ubiquitin is known to be involved in regulating several pathway members, but only *FBXW7* has been previously identified to have a direct role in this pathway (28). In addition, we identified a cluster of three genes associated with sialic acid metabolism (*CMAS, SLC35A1,* and *GNE*) that decreased IRF3 translocation likely secondary to inhibition of SeV entry, as viral load was greatly diminished in these knockouts (Fig. 2*C*), and viral entry is dependent on expression of sialic acids on the cell surface (29). Positive regulators also included many genes not previously associated with IRF3 translocation, including *ATP13A1*, which was one of the top three genes that decreased translocation. *IKBKG* (Nuclear factor kappa B essential modulator, NEMO) knockout also decreased IRF3 translocation and was previously reported to be required for MAVS phosphorylation, which in turn induces IRF3 activation (30). Among putative negative regulators nominated by the screen was the Ragulator complex (*LAMTOR2,3,5* and associated genes *FLCN* and *RRAGC*), which is required for mTOR activation (31) and whose activity was found to increase SeV load (Fig. 2*C*). An mTOR inhibitor, rapamycin, has been shown to increase SeV load in infected cells (32), but the Ragulator complex has not been previously associated with a role in SeV infection or IRF3 activation. Other significant complexes that negatively regulated IRF3 translocation include Mediator-associated genes (*MED13, MED16, MED24, CCNC,* and *BTAF1),* STAGA complex members *(TADA2B, TAF5L,* and *TAF6L),* and components of the HOPS complex (*VPS11, VPS16,* and *VPS39),* which mediates endolysosomal fusion, a process that likely reduces SeV replication as it is inhibited in infected cells (33). Next, we also performed a focused optical pooled screen with the same set of genes upon vesicular stomatitis virus (VSV) infection, in order to determine the effect of each perturbation on IRF3 translocation upon infection with an orthogonal RNA virus, as VSV belongs to a different virus family (Fig. 2 *E* and *F*). Notably, despite reduced effect sizes in the VSV screen, *ATP13A1* and *ATP2B1* decreased IRF3 translocation upon knockout in both settings.

Deep Learning and High-Dimensional Screen Analysis Reveals Gene Functions. In addition to extraction of targeted features such as translocation and intensity from single-cell images, we also input cropped images of individual cells separately for each channel into deep convolutional neural networks (CNNs) to enable unbiased identification of additional features. We extracted features from a CNN pretrained on ImageNet (35) and separately trained an autoencoder on our dataset (Fig. 3*A* and *SI Appendix*, Fig. 2 *A* and *B*). Interestingly, we found that both the features extracted from the pretrained network as well as features defined in the autoencoder's latent representation space identified confirmed hits from the secondary screens with substantially higher accuracy than translocation alone (Fig. 3*B*, ROC AUC improves from 0.71 to as high as 0.93; both CNNs were naive to the secondary screening data). We therefore selected 14 genes predicted to decrease translocation upon knockout by combined autoencoder and transfer learning features that had not scored highly enough to be included in our secondary screens. We found that 8/14 of these genes did indeed decrease translocation via arrayed testing (Fig. 3*C*),
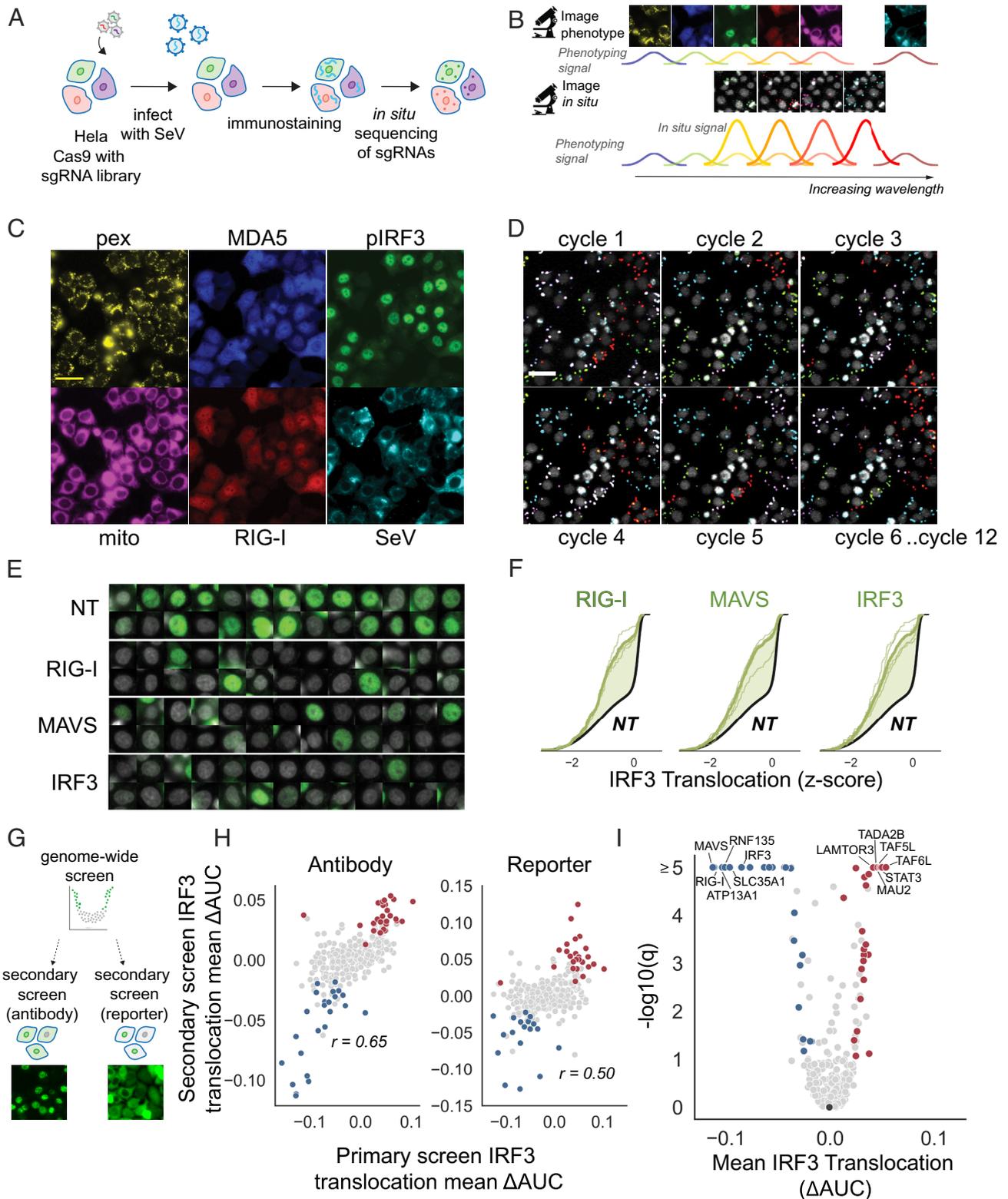
Fig. 1. A genome-wide optical pooled screen reveals regulators of pIRF3 translocation. (*A*) Genome-wide screening workflow. (*B*) Bright in situ signals enable imaging of phenotyping fluorescence signals that overlap with in situ SBS fluorescence signals. (*C*) Example images for each of the six immunofluorescence channels imaged in the genome-wide screen (DAPI was additionally imaged). (Scale bar, 20 μm.) (*D*) First six in situ sequencing cycles (of 12 total cycles) for the same group of cells shown in *C*. (*E*) Single-cell images from genome-wide screen show a decrease in IRF3 translocation in positive control genes. (*F*) Histograms of z-scored IRF3 translocation for positive control genes. Individual traces correspond to unique sgRNAs. (*G*) Hits from the genome-wide screen were assessed using a distinct library of 342 genes with six sgRNAs/gene in two secondary screens with different IRF3 detection assays. (*H*) Secondary translocation screens are well correlated with the primary screen for both antibody staining (r = 0.65, *P* = 2.6e−42) and reporter (r = 0.50, *P* = 5.22e−23). Blue dots indicate significant hits with decreased IRF3 translocation upon knockout, while red dots indicate genes with increased IRF3 translocation. (*I*) Volcano plot of secondary screen results for antibody staining with hits confirmed via secondary screening marked in blue or red. Two-sided *P* values were calculated as described in the *Materials and Methods*, corrected using the Benjamini–Hochberg procedure, and aggregated on the gene level using Fisher's method.
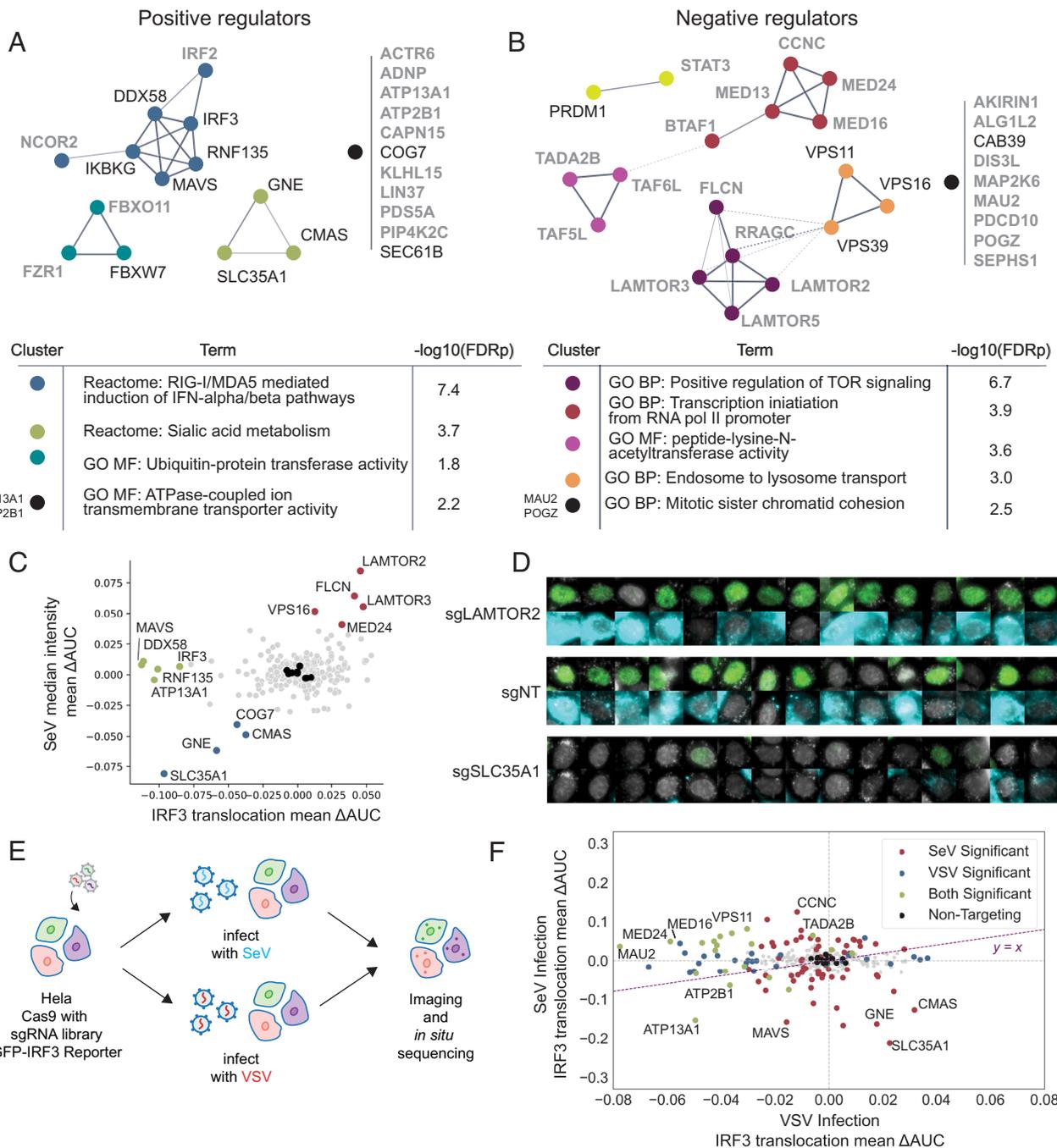
Fig. 2. Analysis of combined hits from secondary screens (*A*). STRING clusters for hits showing decreased translocation using MCL inflation parameter 3 for clustering. Novel genes are in gray, and hits that did not cluster with other hits are listed by the black cluster marker. Table: Top significant GO/Reactome terms associated with each cluster among putative positive regulators. *P* values in *A* and *B* are computed via Enrichr (34) using the Fisher exact test and adjusted using the Benjamini–Hochberg procedure. (*B*) STRING clusters as described in (*A*) for combined hits that increased IRF3 translocation. Table contains top significant GO/Reactome terms associated with each cluster among putative negative regulators. (*C*) IRF3 translocation score plotted against SeV intensity scores for all genes in the antibody staining secondary screen. Black dots indicate nontargeting controls. (*D*) Example single-cell images for nontargeting control cells and the top gene for increased SeV or decreased SeV burden. For each gene/control, pIRF3 staining appears in green in the top row and SeV staining in cyan in the bottom row; each overlaid with DAPI nuclear staining. (*E*) Workflow for secondary screening to assess IRF3 reporter translocation differences upon either Sendai or VSV infection. (*F*) Comparison of per-gene translocation effects between VSV and Sendai virus infections; significance indicates genes with an FDR-adjusted *P* value <0.01.

confirming the hypothesized increased predictiveness of machine learning features even for a defined translocation phenotype.

In addition to IRF3 translocation, we also extracted peroxisome (Fig. 3*D*) and SeV (Fig. 3*G*) intensity features (Dataset S4) from our genome-wide single-cell resolution screen dataset. Our screen also detected genes affecting peroxisomal biogenesis (*PEX13, PEX2, PEX14, PEX1, PEX12, PEX10, PEX6, PEX5, PEX26, PEX11B,* and *PEX3*) as decreasing peroxisome intensity, while known peroxisomal fission genes (*DNM1L* and *MFF*) increased

peroxisomal intensity as expected. Genes showing a decrease in peroxisome intensity selected using peroxisome intensity (targeted), transfer learning, and autoencoder features, all were significantly enriched for the peroxisome GO term (Fig. 3*E*), while genes showing increased peroxisome intensity selected using autoencoder features but not targeted or transfer learning features were significantly enriched for the GO term heme biosynthesis, which has been linked to peroxisome biogenesis through PGC-1α in some studies (36), demonstrating the overlapping but also distinct
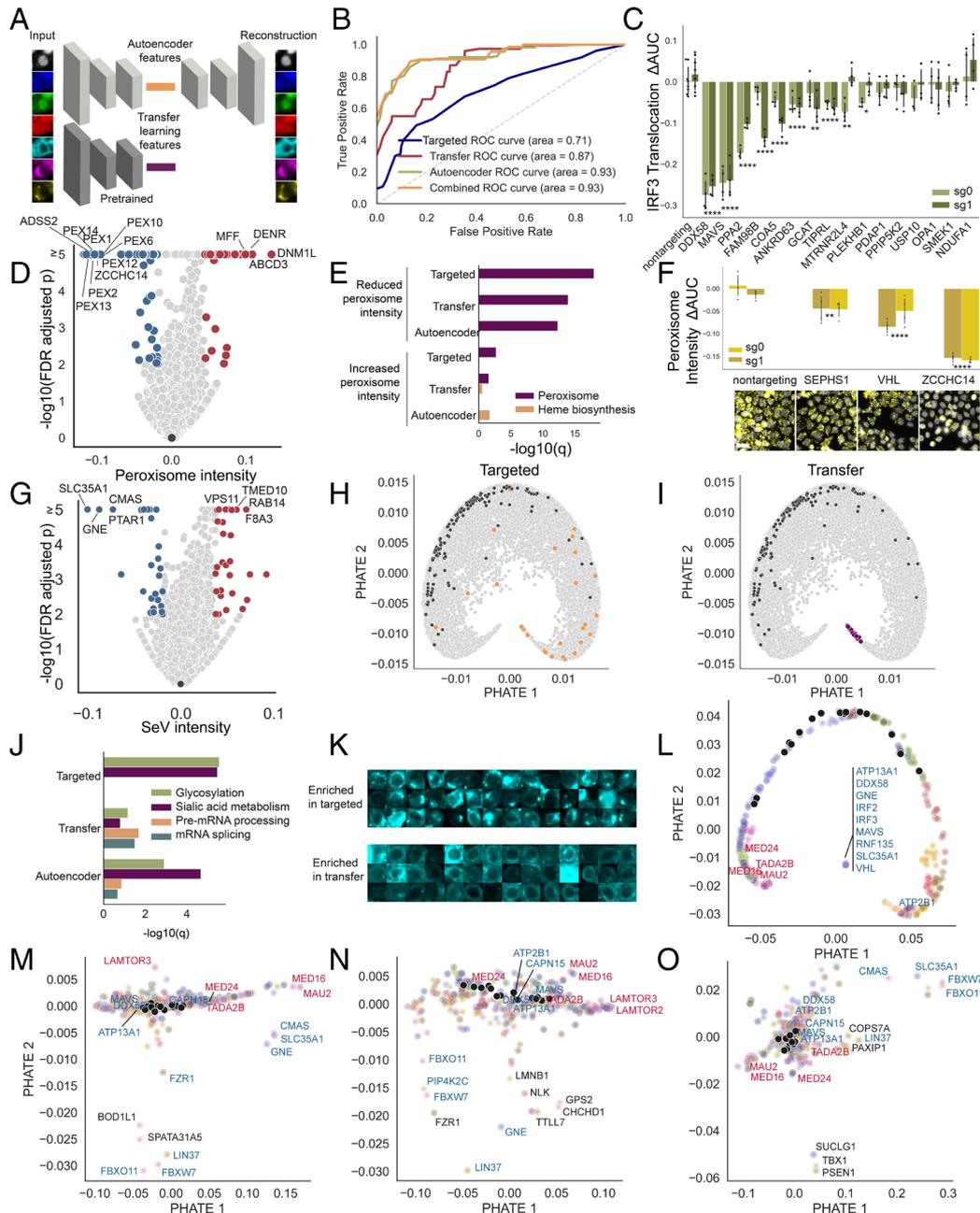
Fig. 3. Deep learning and multidimensional analysis reveal regulators of IRF3, peroxisomes, and SeV. (*A*) Schematic showing extraction of features from representative single-cell crops where each channel is processed by either a pretrained neural network (Xception) or an autoencoder that yielded the example reconstructions shown on the right. (*B*) Both transfer learning and the autoencoder, as well as combined features, improved prediction of true IRF3 translocation hits based on secondary screen results compared to translocation alone using random forest models. (*C*) Eight of fourteen genes predicted to decrease translocation by combined deep learning features showed significantly decreased translocation in arrayed testing with two sgRNAs. *Adjusted $P < 0.05$, **$P < 0.01$, ***$P < 0.001$, and ****$P < 0.0001$. Two-sided P values for *C* and *F* were calculated by computing the delta AUC for the feature of interest between cells in each well and nontargeting control cells (minimum n = 3,000); delta AUCs for all wells containing cells with an sgRNA of interest were then compared to nontargeting delta AUCs using a *t* test; P values were combined using Fisher's method and corrected using the Benjamini–Hochberg procedure. (*D*) Mean peroxisome intensity delta AUC plotted against FDR-adjusted P values for genome-wide screen. Two-sided P values were calculated as described in the *Materials and Methods* and corrected using the Benjamini–Hochberg procedure. (*E*) Genes with reduced peroxisome intensity for targeted, transfer, autoencoder, or all three (13 genes in the Venn diagram in *SI Appendix* Fig. S2C) features showed significant enrichment of GO:0005777 (Peroxisome), while genes showing increased peroxisome intensity based on autoencoder features, unlike targeted features, were enriched for GO:0006783 (heme biosynthesis). Enrichr P values for *E* and *H* are computed using the Fisher exact test and adjusted using the Benjamini–Hochberg procedure. (*F*) Three genes with predicted reduction in peroxisome intensity using two sgRNAs per gene showed decreased peroxisome intensity in arrayed testing. (Scale bar, 20 μm.) *Adjusted $P < 0.05$, **$P < 0.01$, ***$P < 0.001$, and ****$P < 0.0001$. (*G*) Mean SeV intensity delta AUC plotted against FDR-adjusted P values for genome-wide screen. Two-sided P values were calculated as described in the *Materials and Methods* and corrected using the Benjamini–Hochberg procedure. (*H*) PHATE plot of genes derived from transfer learned features from the SeV channel with the top 30 genes that reduced SeV intensity marked in orange (nontargeting controls marked in black). (*I*) Same as (*H*) with the top 30 transfer learned perturbations most distant from nontargeting controls (black points) marked in purple. (*J*) Genes with reduced SeV intensity using targeted and autoencoder features were enriched for R-HSA-446203 (glycosylation) and R-HSA-4085001 (sialic acid metabolism), while genes showing reduced intensity in transfer learning showed stronger enrichment of features related to RNA processing (R-HSA-72203, pre-mRNA processing, and R-HSA-72163, mRNA splicing). (*K*) Images of single cells that scored in the 99th (*Bottom*) or first (*Top*) percentile for the SeV transfer learning feature that most differentiated cells with perturbations shown in purple in panel I from nontargeting control cells. (*L*) PHATE plot of genes in secondary screen clustered using Leiden clustering on autoencoder features from the IRF3 and RIG-I channels, with select genes that decreased IRF3 translocation upon knockout marked with blue text and genes that increased translocation marked in red text; cluster membership is denoted by marker color. (*M*) Same as *L* but using autoencoder features from the Sendai virus channel. (*N*) Same as *L* but using autoencoder features from the nuclei/DAPI channel. (*O*) Same as I but using autoencoder features from the peroxisome channel.

contributions of these three methods of feature extraction. We selected three genes that showed reduced peroxisome intensity using all three feature sets and confirmed via arrayed validation that, even in the absence of SeV, peroxisome intensity was indeed decreased in these genes (Fig. 3F).

We next examined genes that showed changes in SeV intensity in our screen (Fig. 3G). In addition, we analyzed transfer learning and autoencoder features extracted from the Sendai virus channel to identify perturbations that significantly altered Sendai virus subcellular localization. Interestingly, when we performed dimensionality reduction using PHATE (37) on the transfer learned features from the Sendai virus channel, we found that the top 30 genes with decreased Sendai virus intensity (marked in orange in Fig. 3H) did not cluster closely together, indicating that the transfer learned features were capturing significant changes in the Sendai virus images other than changes in our intensity metric. We therefore analyzed the top 30 genes most different from nontargeting controls in the transfer learned features (Fig. 3I). Enrichment analysis of this set showed that genes related to intracellular trafficking (38, 39) scored highly for increased SeV burden (VPS11, RAB14, and TMED10), while genes involved in glycosylation and sialic acid metabolism (SLC35A1, GNE, and CMAS) were highly ranked for a reduction in SeV intensity using targeted and autoencoder features (Fig. 3J). On the other hand, the transfer learning features preferentially identified genes involved in mRNA processing (SART1, NUP155—already shown to interact with Sendai's M protein (40), DHX9—shown to facilitate HIV, HCV, and FMDV replication but not previously associated with SeV (41), and PRPF31), and single-cell images of cells enriched in transfer learning showed diffuse cytoplasmic Sendai antibody staining (Fig. 3 J and K), likely indicating that RNA processing genes required for the formation of cytoplasmic replication foci were not functioning effectively.

We next used features extracted from our autoencoder to cluster genes from our secondary screen. When we clustered genes using features from the IRF3 and RIG-I channels (Fig. 3L), we found that strong positive regulators we had identified (blue text) and negative regulators (red text) clustered apart from nontargeting controls (black); cluster membership indicated by marker colors. When we clustered using features derived from the Sendai virus channel, on the other hand, we found that some of the positive regulators (e.g., MAVS, DDX58, and ATP13A1) did not cause changes in the Sendai channel relative to nontargeting controls (Fig. 3M), while other genes known to be involved in sialic acid biosynthesis and the major negative regulators did alter Sendai virus localization. Interestingly, positive regulators FBXO11 and FBXW7 clustered differently from nontargeting controls in Sendai virus features as well as features from the nuclear and peroxisome channels (Fig. 3 N and O), indicating that apart from their effect on IRF3 translocation, they induce significant cellular perturbations. Notably, genes known to be involved in nuclear organization (LMNB1) or peroxisome-related metabolic processes (SUCLG1) clustered apart from nontargeting controls in only the nuclear or peroxisomal features, respectively.

Arrayed Validation and Transcriptional Analysis of IRF3 Translocation Hits. Following confirmation via secondary screening, we selected seven genes that either decreased (ATP13A1, CAPN15, and ATP2B1) or increased (MAU2, MED16, MED24, and TADA2B) IRF3 translocation when knocked out and confirmed the expected effects on IRF3 translocation via arrayed knockout with two sgRNAs (Fig. 4A, knockout efficiency validated in SI Appendix, Fig. S3, supporting translocation images in SI Appendix, Fig. S4A). We also assayed RIG-I activation (using an antibody against the activated form) and confirmed that 5/7 genes showed differences in RIG-I that paralleled the IRF3 translocation

defect (Fig. 4B). Interestingly, ATP2B1 showed a reduction in IRF3 translocation but an increase in RIG-I activation, indicating that it may regulate a pathway step between RIG-I and IRF3. Next, we assayed the effect of these knockouts in the U937 cell line, a cell model of monocytes, which are critical for the innate immune response. While none of the putative negative regulators significantly altered translocation in U937 cells, all three putative positive regulators reproduced a loss of translocation in these cells (Fig. 4C and SI Appendix, Fig. S4B). Interestingly, the putative negative regulators are all known to modulate transcription, which may be more covariable with changes in the cellular context or the infection time point selected, as we were only able to observe infected U937 cells for a shorter period (7 h) than HeLa cells (15 h) due to high levels of cell death observed at later time points. We next quantified the levels of the active form of RIG-I in HeLa cells in response to a transfected synthetic hairpin RNA (hpRNA) stimulation in order to determine whether altered responses in the context of Sendai infection were secondary to modulation of the infection or, alternatively, were directly regulating antiviral sensing as would be predicted if defects were conserved in response to hpRNA treatment. We again found that responses to knockout of negative regulators were less well conserved, perhaps due to their smaller effect on overall IRF3 translocation (Fig. 4A), and saw no alteration in active RIG-I in these knockouts. However, the two strongest less well-characterized positive regulators, ATP13A1 and CAPN15, reproduced the defect in RIG-I activation in response to hpRNA stimulation (Fig. 4D).

We then performed RNA sequencing of five less well-characterized IRF3 regulators to identify transcriptional effects of these genetic knockouts in an unbiased manner. We found that knockouts of all five regulators had significantly decreased (ATP13A1 and CAPN15) or increased (MED16, MED24, and TADA2B) interferon-stimulated gene (ISG) expression in response to both SeV stimulation at two time points and hpRNA stimulation, in line with their previous observed effects on IRF3 translocation (Fig. 4E). In addition, none of the genes showed significant differences in SeV RNA levels relative to nontargeting controls (SI Appendix, Fig. S4C). Interestingly, a subset of ISGs was up-regulated in ATP13A1 and CAPN15 knockout cells at later infection time points (Fig. 4F). We performed gene set enrichment analysis (GSEA) to further investigate altered pathways in negative regulators of translocation and found that all three had increased serine-type endopeptidase activity (GO:004252), while TADA2B also had increased NOD-like receptor signaling, and both Mediator members had increased lysosomal lumen component RNA expression (Fig. 4G). To further examine positive regulators, we performed gene ontology analysis on genes significantly decreased upon knockout of each regulator relative to both DDX58 and MAVS in the presence of SeV. We found that CAPN15 had significantly decreased expression of nucleolar RNAs and nucleolus components, while among genes with decreased expression in the ATP13A1 knockout, transcripts encoding mitochondrial components were significantly perturbed (Fig. 4H). Finally, we also show that active RIG-I protein is significantly reduced in the absence of ATP13A1 and CAPN15 upon influenza A virus (IAV) infection and for ATP13A1 but not CAPN15 following respiratory syncytial virus (RSV) infection (SI Appendix, Fig. S4 E and F).

MAVS Is Mislocalized in the Absence of Functional ATP13A1. We further tested the putative role of ATP13A1 in regulating IRF3 localization by asking whether ATP13A1 overexpression could rescue appropriate IRF3 translocation. Indeed, we observed restoration of the translocation defect we observed in the knockout when ATP13A1 was overexpressed (Fig. 5A). ATP13A1 encodes a P5A-type ATPase localized to the endoplasmic reticulum (ER) (42, 43) whose yeast homolog spf1 has been shown to be involved in the unfolded protein response (44). However, in our
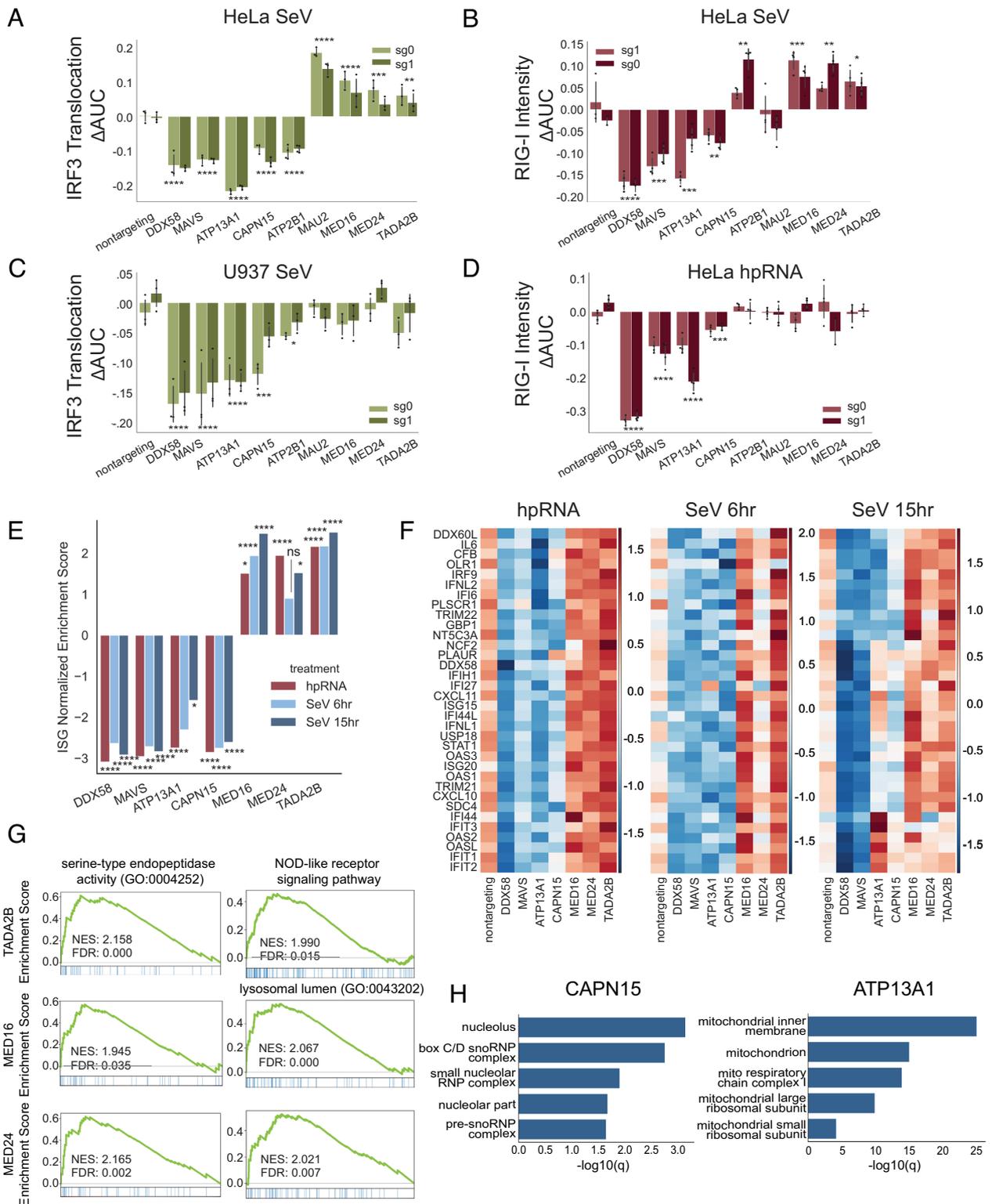
Fig. 4. Arrayed validation and RNA sequencing of IRF3 translocation hits. (*A*) IRF3 translocation in HeLa cells in response to SeV stimulation for the indicated genes. *Adjusted $P < 0.05$, **$P < 0.01$, ***$P < 0.001$, and ****$P < 0.0001$ throughout. Two-sided P values for *A–D* were calculated by computing the delta AUC for the feature of interest between cells in each well and nontargeting control cells (minimum n = 3,000); delta AUCs for all wells containing cells with an sgRNA of interest were then compared to nontargeting delta AUCs using a t test; P values were combined using Fisher's method and corrected using the Benjamini–Hochberg procedure. (*B*) RIG-I activation in HeLa cells in response to SeV stimulation for the indicated genes. (*C*) IRF3 translocation defects in U937 cells in response to SeV stimulation for the indicated genes. (*D*) RIG-I activation in HeLa cells in response to hpRNA stimulation for the indicated genes. (*E*) Normalized enrichment score (NES) computed via GSEA for ISGs (genes significantly enriched in nontargeting control cells with transfected hairpin RNA relative to unstimulated nontargeting control cells). P values were obtained from the gseapy package using 1,000 permutations over all gene sets considered and corrected using the Benjamini–Hochberg procedure. (*F*) Heatmaps showing z-scored gene expression for ISGs in (*E*) in response to hpRNA or SeV treatment for 6 or 15 h. (*G*) GSEA results show increased serine-type endopeptidase activity (*TADA2B, MED16, and MED24*), NOD-like receptor signaling (*TADA2B*), and lysosomal lumen components (*MED16* and *MED24*). P values were obtained from the gseapy package using 1,000 permutations over all gene sets considered and corrected using the Benjamini–Hochberg procedure. (*H*). Enrichr results for genes that were decreased compared to positive controls *DDX58* and *MAVS* in response to SeV stimulation (15 h) show significant enrichment of nucleolus components and small nucleolar RNAs for *CAPN15*, while *ATP13A1* had a significant decrease in mitochondrial components. Enrichr P values are computed using the Fisher exact test and adjusted using the Benjamini–Hochberg procedure.
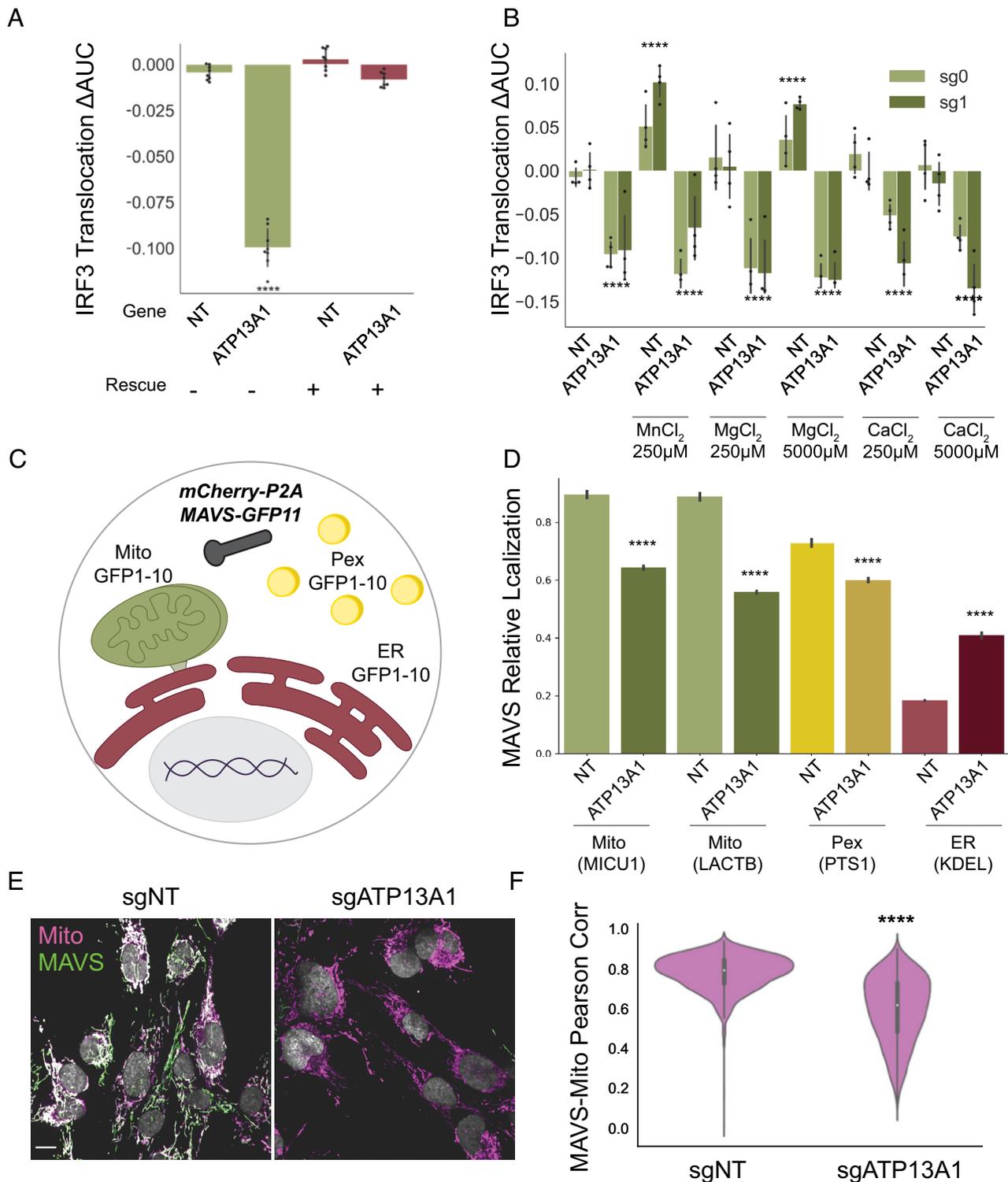
Fig. 5. MAVS is mislocalized in the absence of functional ATP13A1. (*A*) Overexpressed ATP13A1 rescues IRF3 translocation in ATP13A1 knockout HeLa cells. ****$P < 0.0001$. Two-sided P values for *A*, *B*, *D*, and *F* were calculated by computing the delta AUC for the feature of interest between cells in each well and nontargeting control cells (minimum n = 3,000); delta AUCs for all wells containing cells with an sgRNA of interest were then compared to nontargeting delta AUCs using a *t* test; P values were combined using Fisher's method and corrected using the Benjamini–Hochberg procedure. (*B*) IRF3 translocation is not rescued by the addition of exogenous divalent cations in HeLa cells; cytokines added 24 h prior to SeV infection. ****$P < 0.0001$ (*C*) Diagram showing experimental setup for split-GFP experiment, where MAVS is overexpressed in HeLa cells along with either mitochondrial, peroxisomal, or ER GFP1-10. (*D*) In the presence of an ATP13A1 knockout, MAVS targeting to mitochondria and peroxisomes is reduced, while targeting to the ER is increased in HeLa cells. ****$P < 0.0001$. (*E*) In hTERT-immortalized primary BJ1 cells. (Scale bar, 20 μm.) (*F*) Quantification of experiment in (*E*). ****$P < 0.0001$ using a *t* test.

mammalian HeLa *ATP13A1* knockout, we found no increased ER stress (*SI Appendix,* Fig. S5C). A putative transporter, it has been hypothesized to be an ion pump for divalent cations such as manganese, calcium, and magnesium (42, 45); however, adding divalent cations to the culture media did not rescue IRF3

translocation in ATP13A1 knockout cells (Fig. 5B). Recently, *ATP13A1* was shown to be a protein dislocase responsible for the proper targeting of mitochondrial tail-anchored proteins (46). Since MAVS is a tail-anchored mitochondrial protein critical for robust IRF3 translocation, we examined MAVS localization in

ATP13A1 knockout cells, finding that indeed, the fraction of mitochondrial and peroxisomal MAVS was reduced in *ATP13A1* knockout cells, while the fraction of MAVS in the ER was elevated (Fig. 5 *C* and *D*). We further confirmed this effect by examining *MAVS* mitochondrial localization in hTERT-immortalized primary BJ1 cells by confocal microscopy, finding that MAVS mitochondrial localization was greatly reduced in *ATP13A1* knockouts as well as overall MAVS levels, in line with observations from a recent paper (47) (Fig. 5 *E* and *F*).

Discussion

In this study, we applied optical pooled screens at the genome-wide scale, scaling up our original optical pooled screening technology from screens of a few thousand genes to over 20,000. We used the resulting high-dimensional, single-cell resolution dataset to identify regulators of IRF3 subcellular localization. Secondary screens were highly correlated with primary screen data despite modest cellular sampling in the primary screen (median 484 cells per gene), highlighting the remarkable robustness and statistical power achievable with the optical pooled screening method at large scales. A sensitivity analysis (*SI Appendix*, Fig. S11) revealed that for the IRF3 translocation phenotype, an effect size 50% that of strong positive controls could be detected with 200 cells/gene in a genome-wide screen (FDR-adjusted *P* value < 0.001), and 89% of genes in our screen had at least this number of cells. We also applied deep learning analysis to identify latent morphological features in our image-based genome-wide dataset, which helped identify three peroxisome regulators (*VHL, SEPHS1,* and *ZCCHC14*, validated via arrayed knockouts) and a group of RNA processing genes that alter the cytoplasmic localization of SeV.

We confirmed seven regulators of IRF3 translocation via arrayed experiments and investigated five of these regulators through RNA sequencing, confirming expected (signed) differences in ISG induction by SeV. Importantly, we also confirmed ISG induction in response to a synthetic hairpin RNA, showing that these genes indeed act to directly regulate IRF3 pathway induction rather than simply modulating SeV entry or replication. *ATP13A1*, a strong positive regulator that has recently been identified as a mitochondrial tail-anchored protein dislocase (46), resulted in profound loss of IRF3 translocation upon knockout. We hypothesized and confirmed that MAVS, a mitochondrial tail-anchored protein critical for robust IRF3 translocation, is mislocalized in the absence of *ATP13A1*, which results in loss of MAVS from both mitochondrial and peroxisomal membranes with a concomitant increased localization to the ER. We also identified *CAPN15,* a cysteine protease and member of the *SOL* calpain family, as a positive regulator. Little is known about *CAPN15*, whose proteolytic targets have not been identified, but pathogenic variants of the gene result in microphthalmia and cataracts in humans (48). Through RNA sequencing, we found that snoRNP components were down-regulated in the presence of the *CAPN15* knockout. This may decrease snoRNA production, thereby contributing to reduced activation of RIG-I and consequently, IRF3 (49). Among negative regulators, we identified and validated two members of the Mediator complex, *MED16* and *MED24*. In addition to the known role of these Mediator components in transcriptional termination regulation (*SI Appendix*, Fig. S3D) (50), we found that knockouts lead to higher IRF3 translocation and ISG expression and further identified consequences of knockouts using RNA sequencing and pathway analysis. Specifically, we found decreased SUMOylation activity, which negatively regulates IRF3/7 (51), and increased expression of lysosomal lumen components, which can increase antiviral gene expression (52).

In summary, we improved the imaging throughput of optical pooled screening by over fourfold and applied it at the genome-wide scale, discovering positive and negative regulators of viral sensing upstream of IRF3 translocation as well as modulators of SeV protein localization and peroxisomal biogenesis. Optical pooled screening was previously used to assay two to four channels, but here, we image as many as seven channels at a time, enabling a highly multidimensional assessment of spatially defined molecular and cellular morphological features at the single-cell level. As an example, we took advantage of our multidimensional data to identify genes that altered IRF3 translocation without greatly affecting SeV load (Fig. 2*E*), as expected for genes that regulate IRF3 directly. We also identified genes that regulate SeV protein localization, providing a feasible approach to identify host factors affecting viral trafficking and the formation of viral replication foci. Single-cell multichannel images also enable advanced post hoc analysis of the screening data, which we demonstrated here by applying a pretrained neural network model and a second model trained via an autoencoder to extract unbiased feature sets that helped identify regulators of peroxisomes, and factors impacting mRNA processing and SeV localization. The implementation of widely applicable optical pooled screening protocols with increased throughput and phenotype dimensionality—as well as analysis techniques to process the complex datasets produced—will enable many discoveries to be made in future high-dimensional genome-wide optical pooled screens. The results will systematically link genes to important cellular functions and processes by leveraging high-content phenotypic readouts including morphology, subcellular molecule localization, and additional human- and machine-readable molecular and cellular features derived from high-resolution image measures.

Materials and Methods

Library Cloning, Lentivirus Production, Transduction, and Next-Generation Sequencing of Libraries. Libraries were cloned as previously described (21) into a CROP-seq-puro-v2 (Addgene #127458) backbone. Lentivirus was then produced and transduced as previously described (21). For library transductions, multiplicity of infection was estimated by counting colonies after sparse plating and antibiotic selection. Genomic DNA was also extracted for NGS validation of library representation. Genomic DNA was extracted using an extraction mix as described above. Barcodes and sgRNAs were amplified by PCR from a minimum of 100 genomic equivalents per library using JumpStart 2X Master Mix (initial denaturation for 5 min at 98 °C, followed by 28 cycles of annealing for 10 s at 65 °C, extension for 25 s at 72 °C, and denaturation for 20 s at 98 °C).

Sendai Virus Infection, Phenotyping, and In Situ Sequencing for Genome-Wide IRF3 Screen and Secondary Screen. HeLa-TetR-Cas9 cells were transduced with BFP-PTS1, and a single clone expressing the reporter was selected. For screening, cells were selected with puromycin (1 µg/mL) for 3 d after transduction, and library representation was validated by NGS. Cas9 expression was induced with 1 µg/mL doxycycline for 1 wk, and cells were then seeded in six 6-well glass-bottom dishes at 400,000 cells/well 2 d prior to fixation. Sendai virus (Cantell strain, ATCC VR-907) was added at an MOI of 10 in 400 µL media/well for 45 min at 4 °C with rotation; the plate was quickly washed with media, and fresh media added, allowing the virus to replicate for 15 h prior to fixation. Thirty minutes before fixation, 50% of the media was exchanged, and MitoTracker Deep Red added to cells at 37°C at a final concentration of 7 nM. Cells were fixed by removing media and adding 4% paraformaldehyde (Electron Microscopy Sciences 15714) in PBS for 30 min.

Peroxisomes and mitochondria were imaged prior to permeabilization with 100% ice-cold methanol for 20 min. The permeabilization solution was then carefully exchanged with PBS-T wash buffer (PBS + 0.05% Tween-20) by performing six 50% volume exchanges followed by three quick washes. Cells were stained with primary antibodies in 3% BSA (VWR catalog #97061-422) in PBS overnight for pIRF3 (1:250, CST catalog #29047, RRID:AB_2773013), RIG-I

(1:650, AdipoGen catalog #AG-20B-0009, RRID:AB_2490189), and SeV (1:2,500, Abcam catalog #ab33988, RRID:AB_777877) in 1:75 RiboLock, washed 3× in PBS-T, and stained with secondary antibodies for 1 h with 1:1,000 anti-rabbit AF532 (Thermo Fisher Scientific catalog #A-11009, RRID:AB_2534076), 1:1,000 anti-mouse AF594 (Thermo Fisher Scientific catalog #A-21203, RRID:AB_141633), 1:300 anti-chicken DyLight 755 (Thermo Fisher Scientific catalog #SA5-10075, RRID:AB_2556655) in 1:200 RiboLock, washed 6× in PBS-T, and stained with YF488-conjugated anti-MDA5 (1:1,000, custom conjugation of Proteintech catalog #21775-1-AP, RRID:AB_10734593) in 1:200 RiboLock. Cells were then stained with DAPI (500 ng/mL in 2× SSC with 1:75 RiboLock) and imaged.

After phenotyping, the sgRNA sequence was reverse-transcribed in situ for 9.5 h at 37 °C using 1× RevertAid RT buffer, 250 μM dNTPs, 0.2 mg/mL BSA, 1 μM RT primer, 0.8 U/μL RiboLock RNase inhibitor, and 4.8 U/μL RevertAid H minus reverse transcriptase in 750 μL/well. After reverse transcription, cells were washed 5× with PBS-T and postfixed using 3% paraformaldehyde and 0.1% glutaraldehyde in PBS for 30 min, followed by washing with PBS-T three times. Samples were then incubated in a padlock probe and extension–ligation reaction mixture (1× Ampligase buffer, 0.4 U/μL RNase H, 0.2 mg/mL BSA, 100 nM padlock probe, 0.02 U/μL TaqIT polymerase, 0.5 U/μL Ampligase, and 50 nM dNTPs) for 5 min at 37 °C and 90 min at 45 °C and finally washed two times with PBS-T. Circularized padlocks were amplified using a rolling circle amplification mix (1× Phi29 buffer, 250 μM dNTPs, 0.2 mg/mL BSA, 5% glycerol, and 1 U/μL Phi29 DNA polymerase) at 30 °C overnight. In situ sequencing was performed as previously described using sequencing primer oSBS_CROP-seq for 12 cycles. Secondary screening was performed similarly to the genome-wide screen, but phenotyping was restricted to DAPI, pIRF3, RIG-I, and SeV, and seven cycles of in situ sequencing were performed.

Fluorescence Microscopy. All in situ sequencing images were acquired using a Ti-2 Eclipse inverted epifluorescence microscope (Nikon) with automated XYZ stage control and hardware autofocus. An LED light engine (Lumencor CELESTA Light Engine) was used for fluorescence illumination, and all hardware was controlled using NIS-Elements software. In situ sequencing cycles were imaged without filter switching to increase throughput (that is, one channel imaged across the entire plate prior to switching to the subsequent channel) using a 10× 0.45 NA CFI Plan Apo λ objective (Nikon) with the following filters (Semrock) and exposure times for each base: G (546-nm laser at 30% power, emission 575/30 nm, dichroic 552 nm, and 200 ms), T (546-nm laser at 30% power, emission 615/24 nm, dichroic 565 nm, and 200 ms), A (637-nm laser at 30% power, emission 680/42 nm, dichroic 660 nm, and 200 ms), and C (637-nm laser at 30% power, emission 732/68 nm, dichroic 660 nm, and 200 ms). Phenotyping images were also imaged without filter switching and acquired using a 20× 0.75 NA CFI Plan Apo λ objective (Nikon) with the following filters (Semrock unless otherwise noted) and exposure times: BFP-PTS1 (405-nm laser at 10% power, Chroma Multi LED set #89402, 200 ms), DAPI (405-nm laser at 5% power, Chroma Multi LED set #89402, 50 ms), CF488 (477-nm laser at 30% power, Chroma Multi LED set #89402, 200 ms), AF532 (546-nm laser at 10% power, emission 575/30 nm, dichroic 552 nm, and 200 ms), AF594 (546-nm laser at 10% power, emission 615/24 nm, dichroic 565 nm, and 200 ms), MitoTracker Deep Red (637-nm laser at 10% power, emission 680/42 nm, dichroic 660 nm, and 200 ms), and DyLight 755 (749-nm laser at 10% power, emission 820/110 nm, dichroic 765 nm, and 200 ms).

IRF3 Reporter Sendai and VSV Secondary Screen. For live-cell screening, HeLa-TetR-Cas9 cells were transduced with pTRIP-GFP-IRF3 (Addgene #127663). Fluorescent cells were sorted by FACS (Sony SH800) and resorted to select for cells with stable expression. Cells were selected with puromycin (1 μg/mL) for 3 d, and Cas9 expression was induced with 1 μg/mL doxycycline for 1 wk. Cells were then seeded onto 6-well cover glass-bottom plates 2 d prior to translocation experiments. Cells were stimulated with SeV for 15 h or VSV at MOI 2.5 (ATCC catalog #VR-1238) for 18 h prior to fixation with 4% paraformaldehyde for 30 min and initiation of the in situ sequencing protocol. After phenotyping, cells were fixed, and the in situ sequencing protocol (reverse transcription, gap-fill, and rolling circle amplification) was performed, followed by seven bases of SBS.

Arrayed Validation. Top-ranking genes confirmed from the pooled secondary screen were validated with individual sgRNAs. For each gene, two sgRNAs were tested. HeLa-TetR-Cas9 cells expressing pTRIP-GFP-IRF3 (Addgene #127663) were prepared and assayed as in the pooled screen, except that assays were carried out in 96-well glass plates and cells were seeded at 8,000 cells/well. For hpRNA stimulation, cells were seeded in 96-well plates and transfected with 1 μg/mL hpRNA (InvivoGen tlrl-hprna-100) in 10 μL/well LyoVec (InvivoGen lyec-1) for 24 h. For IAV (ATCC catalog #VR-95) and RSV (ATCC catalog #VR-26PQ) infection, cells were treated with virus at an MOI of 1 for 15 h. For arrayed validation of genes with peroxisome defects, HeLa-TetR-Cas9-BFP-PTS1 cells were used. For arrayed validation in U937 cells (ATCC catalog #CRL-1593.2, RRID:CVCL_0007), cells were first transduced with lentiCas9-Blast (Addgene #52962) and selected using 20 μg/mL (Thermo Fisher Scientific A1113903) and then transduced with sgRNAs and selected using 2 μg/mL puromycin (Thermo Fisher Scientific A1113803) for 5 d. Prior to infection with SeV, U937 cells were plated in 96-well plates at 40,000 cells/well with 100 ng/mL PMA (InvivoGen tlrl-pma). After 24 h, PMA was removed, and fresh RPMI with 10% FBS, 1% Pen–Strep was added. Media were again exchanged 24 h after PMA removal, and 41 h after PMA removal, SeV was added at an MOI of 10 to the cells, which were fixed 48 h after PMA removal.

BJ1 MAVS Localization. For experiments with BJ1 cells (BJ-5ta – CRL-4001), cells were transduced with Cas9 and sgRNAs as described for U937 cells but with puromycin selection for 3 d. BJ1 cells were seeded at 8,000 cells/well and stained for mitochondria using MitoTracker Deep Red at 100 nM for 30 min at 37 °C prior to fixation. Cells were permeabilized with ice-cold methanol for 20 min, washed with PBS-T, and stained with a YF488-conjugated MAVS (Proteintech #14341-1-AP, RRID:AB_10548408) at 1:300 for 2 h before imaging. Cells were imaged on an Andor Dragonfly Confocal Microscope.

Split-GFP Localization Experiments. Subcellular localization of MAVS was determined using a split-GFP approach as previously described (53). Targeting sequences for *MICU1* (54)*, LACTB*, and the targeting sequences PTS1 and KDEL (55), GFP1-10 lentiviral vectors were transduced into Cas9-expressing HeLa cells. Transduced cells were transiently transfected with *MICU1*, PTS1, or *VAMP2* GFP11 plasmids to identify cells expressing the mitochondrial, peroxisomal, or ER targeting constructs, respectively, which were isolated via flow cytometry. Cells were then transduced with a full-length mCherry *MAVS* GFP11 lentiviral vector, and MAVS-positive cells were sorted based on mCherry expression. Finally, cells were transduced with a nontargeting or *ATP13A1* sgRNA in the CROP-seq-puro-v2 (Addgene #127458) backbone and selected via puromycin prior to plating and assessment of relative *MAVS* localization.

Indel Sequencing of Arrayed Knockouts. Genomic DNA was extracted as previously described (21), and targeted PCR performed to amplify target gene regions for each sgRNA. Following next-generation sequencing, editing rates were assessed using CRISPResso version 2.038 (56) with parameters –flexiguide_homology 80–quantification_window_size 10 –quantification_window_center -3 –exclude_bp_from_left 0 –exclude_bp_from_right 0.

Western Blotting of ATP13A1 and MAVS. Cells were pelleted and resuspended in lysis buffer (150 mM NaCl, 1% Triton X-100, and 50 mM Tris-HCl, pH 7.5, with one protease inhibitor tablet added to 10 mL buffer, Sigma catalog #11873580001) at 1 million cells per 100 μL. Following incubation for 30 min at 4 °C, lysates were centrifuged at 10,000 × g for 5 min, and supernatant was stored at −80 °C. Lysates were then thawed on ice and Laemmli 6× sample buffer, SDS, reducing (Boston Bioproducts catalog #BP-111R) was added prior to loading on NuPAGE 4 to 12% Bis-Tris Gels (Thermo Fisher catalog #NP0321). Samples were transferred to nitrocellulose membranes using iBlot2 (Thermo Fisher), and blocking was performed in TBS Tween with 5% nonfat milk. Primary antibodies (1:500 ATP13A1 Proteintech catalog #16244-1-AP and 1:1,000 MAVS Proteintech catalog #14341-1-AP) were incubated with samples overnight, and secondary rabbit antibody was added for 1 h prior to visualization with chemiluminescence.

RNA-Seq Analysis of Clonal Knockout Cell Lines. Clonal knockout cell lines and wild-type control cells were plated in 96-well format at a density of 8,000 cells/well. After 24 h, cells were transfected with 1 μg/mL hpRNA (InvivoGen tlrl-hprna-100) in 10 μL/well LyoVec (InvivoGen lyec-1), while cells infected with Sendai virus at an MOI of 10 were infected after 33 and 42 h for 15-h and 6-h Sendai virus incubations. After 48 h, cells were washed with PBS, lysed at room temperature for 5 min in 21 μL TCL buffer (QIAGEN, supplemented with 1% beta-mercaptoethanol) per well, and then stored at −80 °C. Smart-seq2 was performed as described (57). Libraries were sequenced on a NovaSeq 6000 (Illumina) using the v1.0 S4 300-cycle kit (paired end, 150 cycles forward, and 150 cycles reverse).

Quantification and Statistical Analysis.

Image analysis. Images of cell phenotype and in situ sequencing of perturbations were manually aligned during acquisition using nuclear masks to calibrate the plate position to each of the four corner wells during screening. Alignment was then refined computationally via cross-correlation of DAPI across cycles or between individual imaging channels within sequencing cycles since these were acquired separately. For SBS and phenotyping, alignment across channels and imaging acquisitions (12 SBS cycles and two phenotyping acquisitions) were performed using cross-correlation and a high upsample factor (5) to ensure alignment precision. Unlike our previous work, this alignment was then further refined using ORB feature detection (skimage.feature.ORB, n_keypoints = 200 and fast_threshold = 0.05) and RANSAC to filter detected ORB features (skimage.measure.ransac(Euclidean Transform, min_samples = 2, residual_threshold = 1, and max_trials = 200). This allowed for refinement of image alignment and additional image rotation unlike the cross-correlation algorithm which allowed translation alone. Nuclei and cells were detected and segmented as previously described (20). IRF3 translocation was quantified by calculating pixel-wise correlations between the nuclear DAPI channel and the IRF3 channel (reporter or antibody staining). Mitotic cells were removed based on maximum DAPI signal and cell area. In situ sequencing read calling was performed as previously described (20). Data analysis functions were written in Python using Snakemake for workflow control (58).

Optical pooled screen analysis. Cells were segmented by thresholding the DAPI signal to identify nuclei and expanding the resulting regions using the watershed method as previously described (20). Only cells with a minimum of one read matching a barcode in the library were analyzed. Mitotic or apoptotic cells were removed by filtering cells with unusually high or low nuclear/cell area and DAPI signal. IRF3 translocation was calculated by determining the pixel-wise correlation between DAPI and the IRF3 antibody signal or reporter signal within the segmented nuclear area. For the genome-wide screen, only genes with a minimum of one read matching an sgRNA in the library and two sgRNAs with at least 30 cells/sgRNA were considered for analysis. Features were normalized on a per-cell basis relative to nontargeting control cells in the same well by subtracting the median for nontargeting control cells and dividing by the nontargeting control MAD × 1.4826 (59), and scores for features relative to nontargeting controls were determined by calculating differences in cumulative AUCs (shaded area in Fig. 1*F*). These delta AUCs were averaged over sgRNAs for a given gene, and significance was determined by comparing delta AUCs for individual sgRNAs to distributions bootstrapped from nontargeting control cells (bootstrapped 100,000 times). Gene-level p values were aggregated across sgRNAs using Fisher's method and then corrected using the Benjamini–Hochberg procedure.

Deep learning analysis. For both autoencoder and transfer learning, 46 × 46 single-cell cropped images of individual channels were generated for cells whose center was at least 13 pixels away from the nearest cell center. For transfer learning, these single-cell crops were then resized to 299 × 299 images, and each channel was repeated three times to generate 299 × 299 × 3 images of the size required to extract features using the Xception network model (60) provided by Keras. Image intensities were renormalized to be between 0 and 255, and features were extracted from the final layer ("avg_pool") of the Xception network with a feature size of 2048. Features with less than 0.1 coefficient of variation were dropped before further analysis. Only genes with >=30 cells/sgRNA >=2 sgRNAs were considered for further analysis.

The autoencoder model was adapted from a previously published model (61), and the latent feature size was set to 2048. The model was run separately for each channel of the 7-channel image dataset for up to 250 epochs, and the model with the lowest test loss was selected for each channel. The model was trained and tested on 1% of the cells randomly selected from the larger set with 0.25% of the cells as test dataset, and 0.75% were used for training. The trained model was then used to extract latent features from the entire dataset. 2048-length feature vectors for each cell were then combined as described for the transfer learning.

PHATE clustering was performed with knn = 5 and other parameters at default settings, and Leiden clustering performed with resolution = 3.

Arrayed validation. For each sgRNA, the IRF3 translocation or RIG-I activation change was computed relative to nontargeting control cells by computing the difference in AUCs between the cumulative distributions for nontargeting and sgRNA of interest. Delta AUCs for 3 to 4 replicate wells per sgRNA in each experiment were then compared using a t test and corrected using the Benjamini–Hochberg procedure to assess statistical significance.

RNA-seq quantification. Kallisto was used to quantify transcript abundance using AB856846.1 for the Sendai genome. EdgeR was used to assess differential gene expression with default parameters for the estimateDisp and exactTest functions (62, 63). Only transcripts with cpm > 1 in at least two samples were considered. Biological replicates were defined as replicate stimulations with at least two sgRNAs for genes affecting IRF3 translocation. GSEA was performed on VST-transformed data using the DESeq2 package (64). ISGs were defined as genes with minimum expression >3 logCPM that also demonstrated logFC > 3 and FDR < 0.01 between nontargeting unstimulated and nontargeting stimulated with synthetic hpRNA for 24 h.

Data, Materials, and Software Availability. Supplementary datasets 2 and 3 are available at Zenodo (65). Code is available at https://github.com/beccajcarlson/IRF3OpticalPooledScreen (66). RNA-seq data have been deposited in the Gene Expression Omnibus at GSE179288. Image data are publicly available on Google Cloud at gs://opspublic-east1/IRF3OpticalPooledScreen, and one example field of view has been uploaded to the GitHub repository. The BFP-PTS1 plasmid has been deposited to Addgene (#199433).

Author affiliations: [a]Department of Health Sciences and Technology, Massachusetts Institute of Technology, Cambridge, MA 02139; [b]Broad Institute of Massachusetts Institute of Technology and Harvard, Cambridge, MA 02142; [c]Whitehead Institute, Cambridge, MA 02142; [d]Center for Cancer Research, Massachusetts General Hospital, Boston, MA 02114; [e]Department of Biological Engineering, Massachusetts Institute of Technology, Cambridge, MA 02139; and [f]Koch Institute for Integrative Cancer Research at MIT, Cambridge, MA 02139

1. K. T. Chow, M. Gale, Y.-M. Loo, RIG-I and Other RNA Sensors in Antiviral Immunity. *Annu. Rev. Immunol.* **36**, 667–694 (2018).
2. I. Buers, Y. Nitschke, F. Rutsch, Novel interferonopathies associated with mutations in RIG-I like receptors. *Cytokine Growth Factor Rev.* **29**, 101–107 (2016).
3. Y. J. Crow, N. Manel, Aicardi-Goutières syndrome and the type I interferonopathies. *Nat. Rev. Immunol.* **15**, 429–440 (2015).
4. X. Jiang *et al.*, Intratumoral delivery of RIG-I agonist SLR14 induces robust antitumor responses. *J. Exp. Med.* **216**, 2854–2868 (2019).
5. J. Baggen *et al.*, Genome-wide CRISPR screening identifies TMEM106B as a proviral host factor for SARS-CoV-2. *Nat. Genet.* **53**, 435–444 (2021).
6. Z. Daniloski *et al.*, Identification of Required Host Factors for SARS-CoV-2 Infection in Human Cells. *Cell* **184**, 92–105.e16 (2021).
7. S. Ding *et al.*, STAG2 deficiency induces interferon responses via cGAS-STING pathway and restricts virus infection. *Nat. Commun.* **9**, 1485 (2018).
8. M. Flint *et al.*, A genome-wide CRISPR screen identifies N-acetylglucosamine-1-phosphate transferase as a potential antiviral target for Ebola virus. *Nat. Commun.* **10**, 285 (2019).
9. Y. Li *et al.*, Genome-wide CRISPR screen for Zika virus resistance in human neural cells. *Proc. Natl. Acad. Sci. U.S.A.* **116**, 9527–9532 (2019).
10. W. M. Schneider *et al.*, Genome-Scale Identification of SARS-CoV-2 and Pan-coronavirus Host Factor Networks. *Cell* **184**, 120–132.e14 (2021).

11. R. Wang et al., Genetic Screens Identify Host Factors for SARS-CoV-2 and Common Cold Coronaviruses. Cell 184, 106–119.e14 (2021).
12. Y. Zhu et al., A genome-wide CRISPR screen identifies host factors that regulate SARS-CoV-2 entry. Nat. Commun. 12, 961 (2021).
13. B. Li et al., Genome-wide CRISPR screen identifies host dependency factors for influenza A virus infection. Nat. Commun. 11, 164 (2020).
14. R. B. Richardson et al., A CRISPR screen identifies IFI6 as an ER-resident interferon effector that blocks flavivirus replication. Nat. Microbiol. 3, 1214–1223 (2018).
15. J. Börold et al., BRD9 is a druggable component of interferon-stimulated gene expression and antiviral activity. EMBO Rep. 22, e52823. (2021).
16. A. T. Harding, M. A. Goff, H. M. Froggatt, J. K. Lim, N. S. Heaton, GPER1 is required to protect fetal health from maternal inflammation. Science 371, 271–276 (2021).
17. J. H. Lumb et al., DDX6 Represses Aberrant Activation of Interferon-Stimulated Genes. Cell Rep. 20, 819–831 (2017).
18. M. Baril et al., Genome-wide RNAi Screen Reveals a New Role of a WNT/CTNNB1 Signaling Pathway as Negative Regulator of Virus-induced Innate Immune Responses. PLOS Pathog. 9, e1003416. (2013).
19. J. Willemsen et al., Phosphorylation-Dependent Feedback Inhibition of RIG-I by DAPK1 Identified by Kinome-wide siRNA Screening. Mol. Cell 65, 403–415.e8 (2017).
20. D. Feldman et al., Optical Pooled Screens in Human Cells. Cell 179, 787–799.e17 (2019).
21. D. Feldman et al., Pooled genetic perturbation screens with image-based phenotypes. Nat. Protoc. 17, 476–512 (2022).
22. L. Funk et al., The phenotypic landscape of essential human genes. Cell (2022).
23. J. R. Bedsaul, L. A. Zaritsky, K. C. Zoon, Type I Interferon-Mediated Induction of Antiviral Genes and Proteins Fails to Protect Cells from the Cytopathic Effects of Sendai Virus Infection. J. Interferon Cytokine Res. 36, 652–665 (2016).
24. E. Dixit et al., Peroxisomes are signaling platforms for antiviral innate immunity. Cell 141, 668–681 (2010).
25. R. Ke et al., In situ sequencing for RNA analysis in preserved tissue and cells. Nat. Methods 10, 857–860 (2013).
26. J. Rehwinkel, M. U. Gack, RIG-I-like receptors: their regulation and roles in RNA sensing. Nat. Rev. Immunol. 20, 537–551 (2020).
27. D. Szklarczyk et al., STRING v11: protein-protein association networks with increased coverage, supporting functional discovery in genome-wide experimental datasets. Nucleic Acids Res. 47, D607–D613 (2019).
28. Y. Song et al., E3 ligase FBXW7 is critical for RIG-I stabilization during antiviral responses. Nat. Commun. 8, 14654 (2017).
29. M. A. Markwell, J. C. Paulson, Sendai virus utilizes specific sialyloligosaccharides as host cell receptor determinants. Proc. Natl. Acad. Sci. U.S.A. 77, 5693–5697 (1980).
30. S. Liu et al., Phosphorylation of innate immune adaptor proteins MAVS, STING, and TRIF induces IRF3 activation. Science 347, aaa2630 (2015).
31. Y. Sancak et al., Ragulator-Rag Complex Targets mTORC1 to the Lysosomal Surface and Is Necessary for Its Activation by Amino Acids. Cell 141, 290–303 (2010).
32. G. Subramanian et al., A new mechanism of interferon's antiviral action: Induction of autophagy, essential for paramyxovirus replication, is inhibited by the interferon stimulated gene, TDRD7. PLOS Pathog. 14, e1006877. (2018).
33. A. L. Wozniak, A. Long, K. N. Jones-Jamtgaard, S. A. Weinman, Hepatitis C virus promotes virion secretion through cleavage of the Rab7 adaptor protein RILP. Proc. Natl. Acad. Sci. U.S.A. 113, 12484–12489 (2016).
34. M. V. Kuleshov et al., Enrichr: a comprehensive gene set enrichment analysis web server 2016 update. Nucleic Acids Res. 44, W90–97 (2016).
35. J. Deng et al., ImageNet: A large-scale hierarchical image database in 2009 IEEE Conference on Computer Vision and Pattern Recognition (2009), pp. 248–255.
36. C. Handschin et al., Nutritional regulation of hepatic heme biosynthesis and porphyria through PGC-1alpha. Cell 122, 505–515 (2005).
37. K. R. Moon et al., Visualizing structure and transitions in high-dimensional biological data. Nat. Biotechnol. 37, 1482–1492 (2019).
38. M. S. Deffieu et al., Rab7-harboring vesicles are carriers of the transferrin receptor through the biosynthetic secretory pathway. Sci. Adv. 7, eaba7803 (2021).
39. A. Kehl et al., A trafficome-wide RNAi screen reveals deployment of early and late secretory host proteins and the entire late endo-/lysosomal vesicle fusion machinery by intracellular Salmonella. PLoS Pathog. 16, e1008220. (2020).
40. M. Pentecost et al., Evidence for Ubiquitin-Regulated Nuclear and Subnuclear Trafficking among Paramyxovirinae Matrix Proteins. PLOS Pathog. 11, e1004739. (2015).
41. A. Fullam, M. Schröder, DExD/H-box RNA helicases as mediators of anti-viral innate immunity and essential host factors for viral replication. Biochim. Biophys. Acta Gene Regul. Mech. 1829, 854–865 (2013).
42. Y. Cohen et al., The Yeast P5 Type ATPase, Spf1, Regulates Manganese Transport into the Endoplasmic Reticulum. PLoS One 8 (2013).
43. D. M. Sørensen et al., Parkinson disease related ATP13A2 evolved early in animal evolution. PLOS One 13, e0193228. (2018).
44. M. C. Jonikas et al., Comprehensive Characterization of Genes Required for Protein Folding in the Endoplasmic Reticulum. Science 323, 1693–1697 (2009).
45. D. M. Sørensen, M. J. Buch-Pedersen, M. G. Palmgren, Towards defining the substrate of orphan P5A-ATPases. Biochim. Biophys. Acta BBA - Gen. Subj. 1850, 524–535 (2015).
46. M. J. McKenna et al., The endoplasmic reticulum P5A-ATPase is a transmembrane helix dislocase. Science 369 (2020).
47. M. J. McKenna, B. M. Adams, V. Chu, J. A. Paulo, S. Shao, ATP13A1 prevents ERAD of folding-competent mislocalized and misoriented proteins. Mol. Cell 82, 4277–4289.e10 (2022).
48. H. Mor-Shaked et al., Biallelic deletion in a minimal CAPN15 intron in siblings with a recognizable syndrome of congenital malformations and developmental delay. Clin. Genet. 99, 577–582 (2021).
49. J. J. Chiang et al., Viral unmasking of cellular 5S rRNA pseudogene transcripts induces RIG-I mediated immunity. Nat. Immunol. 19, 53–62 (2018).
50. H. Takahashi et al., The role of Mediator and Little Elongation Complex in transcription termination. Nat. Commun. 11, 1063 (2020).
51. T. Kubota et al., Virus Infection Triggers SUMOylation of IRF3 and IRF7, Leading to the Negative Regulation of Type I Interferon Gene Expression. J. Biol. Chem. 283, 25660–25670 (2008).
52. M. Hasan et al., Trex1 regulates lysosomal biogenesis and interferon-independent activation of antiviral genes. Nat. Immunol. 14, 61–71 (2013).
53. S.-I. Hyun, L. Maruri-Avidal, B. Moss, Topology of Endoplasmic Reticulum-Associated Cellular and Viral Proteins Determined with Split-GFP. Traffic Cph. Den. 16, 787–795 (2015).
54. M. Le Vasseur et al., Genome-wide CRISPRi screening identifies OCIAD1 as a prohibitin client and regulatory determinant of mitochondrial Complex III assembly in human cells. eLife 10, e67624. (2021).
55. A. J. Inglis, K. R. Page, A. Guna, R. M. Voorhees, Differential Modes of Orphan Subunit Recognition for the WRB/CAML Complex. Cell Rep. 30, 3691–3698.e5 (2020).
56. L. Pinello et al., Analyzing CRISPR genome-editing experiments with CRISPResso. Nat. Biotechnol. 34, 695–697 (2016).
57. J. J. Trombetta et al., Preparation of Single-Cell RNA-Seq Libraries for Next Generation Sequencing. Curr. Protoc. Mol. Biol. 107, 4.22.1-17 (2014).
58. J. Köster, S. Rahmann, Snakemake–a scalable bioinformatics workflow engine. Bioinformatics 28, 2520–2522 (2012).
59. M.-A. Bray et al., Cell Painting, a high-content image-based assay for morphological profiling using multiplexed fluorescent dyes. Nat. Protoc. 11, 1757–1774 (2016).
60. F. Chollet, Xception: Deep Learning with Depthwise Separable Convolutions. ArXiv161002357 Cs (2017) (Accessed June 24, 2021).
61. K. D. Yang et al., Predicting cell lineages using autoencoders and optimal transport. PLOS Comput. Biol. 16, e1007828. (2020).
62. N. L. Bray, H. Pimentel, P. Melsted, L. Pachter, Near-optimal probabilistic RNA-seq quantification. Nat. Biotechnol. 34, 525–527 (2016).
63. M. D. Robinson, D. J. McCarthy, G. K. Smyth, edgeR: a Bioconductor package for differential expression analysis of digital gene expression data. Bioinformatics 26, 139–140 (2010).
64. M. I. Love, W. Huber, S. Anders, Moderated estimation of fold change and dispersion for RNA-seq data with DESeq2. Genome Biol. 15, 550 (2014).
65. R. J. Carlson et al., A genome-wide optical pooled screen reveals regulators of cellular antiviral responses: Data, Zenodo. https://doi.org/10.5281/zenodo.5013414. Deposited 17 March 2023.
66. R. J. Carlson et al., A genome-wide optical pooled screen reveals regulators of cellular antiviral responses: Code, Zenodo. https://doi.org/10.5281/zenodo.7775042. Deposited 27 March 2023.